RESEARCH ARTICLE

ADVANCED THEORY AND SIMULATIONS
www.advtheorysimul.com

Collective Motion of Quincke Rollers with Fully Resolved Hydrodynamics

Shun Imamura, Kohei Sawaki, John J. Molina, Matthew S. Turner, and Ryoichi Yamamoto**

Hydrodynamic effects are known to significantly affect the collective behavior of wet active matter systems. However, the non-linear many-body nature of these interactions makes them very challenging to analyze, particularly in dense suspensions. Quincke rollers are one of the canonical examples of artificial microswimmers. These are active particles that move freely above a plate due to the torque generated by a uniform DC electric field. A system involving many such particles exhibits a variety of collective dynamics, such as the disordered gas, polar liquid, and active crystal states. This work accomplishes numerical simulations of a 3D system containing many rollers in order to explicitly resolve the hydrodynamic interactions and understand the role these play in the resulting active dynamics. It reveals that the far-field hydrodynamic effects tend to drive ordered collective motion, while the near-field effects tend to drive disordered collective behavior, and reproduce diverse collective behavior while capturing the role of hydrodynamic effects between rollers without resorting to the approximations previously employed.

1. Introduction

Active matter has been typically classified in terms of wet or dry, biological or non-living. Most well known biological examples are wet, for example, bacteria, spermatozoa, and algae, which means that hydrodynamic interactions (HIs) should be taken into account to provide a complete description of their behavior. Unfortunately, performing detailed experimental measurements is difficult. Thus, artificial microswimmers have quickly become an important system for investigating the role of HIs, in particular, to understand the origins of the various modes of collective motion that have been observed and/or predicted.[1–5] Among them, a microroller is a physically simple microswimmer for studying the dynamic self-assembly of non-equilibrium systems, and their behavior has been shown to have a deep relationship to that of the flocks of fish, bacteria, and other biological systems, through recently developed theoretical models.[6–8] Microrollers controlled by electric fields are called as Quincke rollers, and their various collective behaviors are known to be produced by hydrodynamic and electrostatic couplings.[9] However, although the hydrodynamic effects are known to play a crucial role, the precise manner in which they control the dynamics of many-body systems, and the relative importance of near-field interactions, have not yet been fully resolved.

When a uniform DC electric field is applied to a dielectric particle in an electrolyte fluid, spontaneous rotation of the particle can be observed due to an electrohydrodynamic instability known as the Quincke effect[10] (see **Figure 1**). A Quincke roller is a self-propelled particle whose propulsion is driven by the hydrodynamic traction force exerted on a particle rotating due to the Quincke effect near a substrate.[9] The propulsion velocity of the roller is proportional to the angular velocity, which can be controlled via the magnitude of the external electric field.[11,12]

A variety of distinct regimes have been observed in experimental studies, including gas, polar liquid, active solid and cluster states,[9,13–18] as well as an order–disorder transition between the polar liquid and gas states,[9] mobility enhancement due to paired-up states,[13] and solidification at high density.[15] Numerical studies have also been conducted, mostly using 2D particle-based models. These have had partial success in reproducing some experimental observations.[9,16] The far-field HI between Quincke rollers has been considered using Stokesian dynamics.[19–21] A continuum model has also been used to investigate the linear stability of the liquid–solid flocking transition.[9,15] In previous numerical studies, the near-field HIs have been greatly simplified, being computed as the superposition of two-body interactions, with the fluid flow around the rollers treated implicitly, even for dense systems, where a more faithful treatment of the lubrication effect between rotating particles becomes essential. In the present work we have computed the fluid flow around the rollers explicitly, so that the many-body HIs can be accurately calculated for dense dispersions. The only approximations we rely on are: 1) the use of a finite width particle/fluid interface; and 2) the discretization of space and time inherent to all direct numerical simulations. However, in contrast

S. Imamura, K. Sawaki, J. J. Molina, M. S. Turner, R. Yamamoto
Department of Chemical Engineering
Kyoto University
Kyoto 615-8510, Japan
E-mail: imamura@cheme.kyoto-u.ac.jp; ryoichi@cheme.kyoto-u.ac.jp

M. S. Turner
Department of Physics
University of Warwick
Coventry CV4 7AL, UK

The ORCID identification number(s) for the author(s) of this article can be found under https://doi.org/10.1002/adts.202200683

DOI: 10.1002/adts.202200683

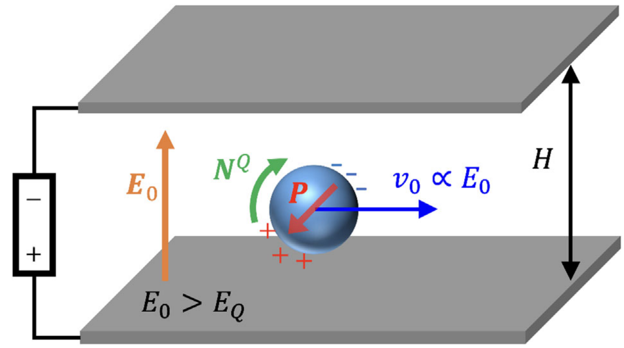

Figure 1. A schematic illustration of a Quincke roller. When a DC electric field E_0 (greater than a threshold E_Q) is applied to a dielectric particle located near the lower of two plates in an electrolyte fluid, the particle spontaneously rotates and is propelled to move on the plate due to an electrohydrodynamic instability called the Quincke effect. Here, $\boldsymbol{P}$ is the induced electric dipole moment, $\boldsymbol{N}^Q \propto \boldsymbol{P} \times \boldsymbol{E}_0$ is the electric torque exerted due to the Quincke effect, $v_0 \propto E_0$ is the propulsion velocity, and H is the distance between the lower and upper electrode plates.

to other techniques, our method directly solves the Navier–Stokes equation under the physically relevant boundary conditions, and is guaranteed to converge to the real solutions in the limit when the grid spacing goes to zero.

In this paper, we report direct numerical simulations (DNS) of a 3D system containing many self-rotating particles in which we explicitly resolve the HIs between them. We first present the details of our numerical implementation method, then we test the validity of the present DNS method by comparing our results with theoretical predictions for a single particle system. The role and importance of the near-field hydrodynamics are then examined for 2- and 3-body systems, where we find that these are determined by a balance between HIs and dipolar interactions. Finally, we present a comprehensive analysis of our DNS results for many-particle systems. Here the collective motion depends on the magnitude of the applied electric field, which changes the induced dipole moments and the angular speed for Quincke rotation, the area fraction of the particles, and the strength of the interparticle attraction.

2. Smoothed Profile Method

Many computational simulation methods that include HIs have been proposed for systems that consist of microswimmers.[22] One example is the smoothed profile (SP) method. This has been applied to study the structure and dynamics in a variety of particle dispersions, such as colloidal systems and self-propelled microswimmers.[23] The SP method can describe both near-field and far-field hydrodynamic effects reasonably accurately and is applicable to dense systems.[24,25] Here, we use dimensionless simulation units throughout, the length is given by the grid spacing, the time, and the energy by the fluid density and the fluid viscosity, and the electric dipole by the dielectric constant in a vacuum.

The presence of the i-th particle is described by the SP function ϕ_i, which takes values of $\phi_i = 1$ in the solid domain and $\phi_i = 0$ in the fluid domain. These domains are smoothly connected by an interface of finite width ξ at the particle surface.[24] In the SP method, the velocity field $\boldsymbol{u}$ is defined at all positions $\boldsymbol{x}$ and times t so as to interpolate between the host fluid, moving with velocity $\boldsymbol{u}_\mathrm{f}$, and the solid particle domain moving with velocity$\boldsymbol{u}_\mathrm{p}$,

$$\boldsymbol{u}(\boldsymbol{x},t) = (1-\phi)\boldsymbol{u}_f(\boldsymbol{x},t) + \phi\boldsymbol{u}_p(\boldsymbol{x},t) \tag{1}$$

In the equation above, the particle field ϕ is to be treated as a sum over the contribution of all particles. The two terms in Equation (1) are defined as

$$(1-\phi)\boldsymbol{u}_\mathrm{f}(\boldsymbol{x},t) = \left(1-\sum_{i=1}^{N}\phi_i(\boldsymbol{x},t)\right)\boldsymbol{u}_\mathrm{f}(\boldsymbol{x},t) \tag{2}$$

and

$$\phi\boldsymbol{u}_\mathrm{p}(\boldsymbol{x},t) = \sum_{i=1}^{N}\phi_i(\boldsymbol{x},t)(\boldsymbol{V}_i + \boldsymbol{\Omega}_i \times \boldsymbol{r}_i) \tag{3}$$

where $\boldsymbol{r}_i = \boldsymbol{x} - \boldsymbol{R}_i$ is a radial vector originating at the center of the i-th particle, with $\boldsymbol{R}_i$ that particle's center, $\boldsymbol{V}_i$ its velocity, and $\boldsymbol{\Omega}_i$ its angular velocity. The total particle phase-field $\phi(\boldsymbol{x},t)$ is defined as the superposition of the SP functions of all particles.

The fluid velocity $\boldsymbol{u}_\mathrm{f}$ satisfies the incompressible Navier–Stokes equation,

$$\left(\partial_t + \boldsymbol{u}_\mathrm{f}\cdot\boldsymbol{\nabla}\right)\boldsymbol{u}_\mathrm{f} = \rho_\mathrm{f}^{-1}\boldsymbol{\nabla}\cdot\boldsymbol{\sigma}_f \tag{4}$$

$$\boldsymbol{\nabla}\cdot\boldsymbol{u}_\mathrm{f} = 0 \tag{5}$$

$$\boldsymbol{\sigma}_f = -p\mathrm{I} + \eta_\mathrm{f}\left[\boldsymbol{\nabla}\boldsymbol{u}_\mathrm{f} + \left(\boldsymbol{\nabla}\boldsymbol{u}_\mathrm{f}\right)^\mathrm{T}\right] \tag{6}$$

where $\rho_\mathrm{f}, \eta_\mathrm{f}$, and $\boldsymbol{\sigma}_\mathrm{f}$ are the mass density, viscosity, and stress of the fluid; p is the pressure; I is the unit tensor; and $(\cdots)^T$ indicates a transpose. The total velocity field $\boldsymbol{u}$ is then governed by a modified Navier–Stokes equation, together with the incompressibility condition:[23,24]

$$(\partial_t + \boldsymbol{u}\cdot\boldsymbol{\nabla})\boldsymbol{u} = \rho_f^{-1}\boldsymbol{\nabla}\cdot\boldsymbol{\sigma} + \phi\boldsymbol{f}_\mathrm{p} \tag{7}$$

$$\boldsymbol{\nabla}\cdot\boldsymbol{u} = 0 \tag{8}$$

where the rigidity of the particle domain is maintained by the force density field $\rho_f\phi\boldsymbol{f}_p(\boldsymbol{x},t)$, which is computed to ensure momentum conservation between the fluid domain and the rigid-body domain of the particles. The stress $\boldsymbol{\sigma}$ is defined as in Equation (6), but in terms of the total velocity field $\boldsymbol{u}$. Note that all quantities (fluid/particle) are now defined over the entire computational domain, allowing for efficient numerical calculations (see Appendix C for details).

The motion of the Quincke rollers is determined by the Newton–Euler equations of motion:

$$\frac{\mathrm{d}\boldsymbol{R}_i}{\mathrm{d}t} = \boldsymbol{V}_i, \tag{9}$$

$$M\frac{\mathrm{d}\boldsymbol{V}_i}{\mathrm{d}t} = \boldsymbol{F}_i^\mathrm{H} + \boldsymbol{F}_i^\mathrm{P} + \boldsymbol{F}_i^\mathrm{E}, \tag{10}$$

$$\frac{\mathrm{d}\boldsymbol{Q}_i}{\mathrm{d}t} = \mathrm{skew}(\boldsymbol{\Omega}_i)\cdot\boldsymbol{Q}_i \tag{11}$$

$$\boldsymbol{I}\cdot\frac{\mathrm{d}\boldsymbol{\Omega}_i}{\mathrm{d}t} = \boldsymbol{N}_i^\mathrm{H} + \boldsymbol{N}_i^\mathrm{P} + \boldsymbol{N}_i^\mathrm{Q} + \boldsymbol{N}_i^\mathrm{C}, \tag{12}$$

where $M = 4\pi a^3 \rho_\mathrm{p}/3$ is the mass of a particle, $\boldsymbol{Q}$ is the particle's rotation matrix (skew($\boldsymbol{\Omega}$) is the skew-symmetric angular velocity matrix), $\boldsymbol{I} = 2a^2 M\mathrm{I}/5$ is the moment of inertia, a is the particle radius, and ρ_p is the particle density.

The hydrodynamic forces and torques due to the fluid-particle interactions are denoted as $\boldsymbol{F}_i^\mathrm{H}$ and $\boldsymbol{N}_i^\mathrm{H}$, respectively. To compute the hydrodynamic forces and torques, we first partially update the velocity field, from $\boldsymbol{u}$ to $\boldsymbol{u}^\star$, by solving the Navier–Stokes equation, Equation (7), for the advection and viscous stress terms (i.e., without the penalty force term $\phi \boldsymbol{f}_\mathrm{p}$). Then, assuming momentum conservation between the particle and fluid domains, the hydrodynamic forces and torques are defined in terms of the corresponding momentum impulses over the spatial domains of each of the particles[23,24]

$$\int_t^{t+\Delta t} \boldsymbol{F}_i^\mathrm{H} \mathrm{d}t' = \int \rho_\mathrm{f} \phi_i (\boldsymbol{u}^\star - \boldsymbol{u}_p) \mathrm{d}\boldsymbol{x} \tag{13}$$

$$\int_t^{t+\Delta t} \boldsymbol{N}_i^\mathrm{H} \mathrm{d}t' = \int \boldsymbol{r}_i \times \rho_\mathrm{f} \phi_i (\boldsymbol{u}^\star - \boldsymbol{u}_\mathrm{p}) \mathrm{d}\boldsymbol{x} \tag{14}$$

where Δt is the computational time increment and the spatial integration is over all space. These forces (torques) are used to update the velocities of the rigid-particles. The penalty force $\phi \boldsymbol{f}_\mathrm{p}$ is defined in such a way that the final velocity field $\boldsymbol{u} = \boldsymbol{u}^\star + \int \mathrm{d}t' \phi \boldsymbol{f}_\mathrm{p}$, satisfies the rigid-body constraints over the particle domain, consistent with the updated particle velocities and the divergence-free condition. A detailed description of this fractional-step approach is given in Appendix C. The forces and torques due to the interparticle interactions, $\boldsymbol{F}_i^\mathrm{P}$ and $\boldsymbol{N}_i^\mathrm{P}$, are derived from an interaction potential $U = U^\mathrm{D} + U^\mathrm{S} + U^\mathrm{A}$, which is assumed to be pairwise additive[26] (see Appendix A). The corresponding potential between a pair of particles i and j, with dipole moments $\boldsymbol{P}_i$ and $\boldsymbol{P}_j$ and separation $\boldsymbol{r} = \boldsymbol{R}_j - \boldsymbol{R}_i$ is

$$U_{ij}^\mathrm{D}(\boldsymbol{r}, \boldsymbol{P}_i, \boldsymbol{P}_j) = \frac{1}{4\pi\epsilon_0}\left[\frac{\boldsymbol{P}_i \cdot \boldsymbol{P}_j}{r^3} - 3\frac{(\boldsymbol{P}_i \cdot \boldsymbol{r})(\boldsymbol{P}_j \cdot \boldsymbol{r})}{r^5}\right] \tag{15}$$

$$U_{ij}^\mathrm{S}(r) = 4\epsilon^\mathrm{LJ}\left[\left(\frac{\sigma}{r}\right)^{36} - \left(\frac{\sigma}{r}\right)^{18}\right] + \epsilon^{LJ} \tag{16}$$

$$U_{ij}^\mathrm{A}(r) = -\epsilon^\mathrm{A} \exp\left(-\kappa r\right)/r^2 \tag{17}$$

where the U_{ij}^D represents the electrostatic dipole–dipole interactions and includes the interactions of the image dipoles,[9] and these electrostatic interactions are calculated via the Ewald method.[27–29]

The induced electric dipole is decomposed into the components parallel and perpendicular to the wall, as $\boldsymbol{P} = P_\parallel \boldsymbol{e}'_y + P_\perp \boldsymbol{e}'_z$, where $\{\boldsymbol{e}'_x, \boldsymbol{e}'_y, \boldsymbol{e}'_z = \boldsymbol{e}_z\}$ define a time-dependent orthonormal basis (the Quincke-frame). Physically, $P_\parallel$ gives the dipole–dipole interaction within the plane, and $P_\perp$ gives an isotropic repulsion.[9] This dipole causes the Quincke rotation due to the electric torque $\boldsymbol{N}_i^\mathrm{Q} = \boldsymbol{P}_i \times \boldsymbol{E}_0$, which by definition will be parallel to $\boldsymbol{e}'_x$, $\boldsymbol{\Omega}_0 = \Omega_0 \boldsymbol{e}'_x$. The initial orientation for $\boldsymbol{P}$ will be determined by a small perturbation in the surface charge distribution, giving rise to a symmetry breaking.[9,11] To mimic this spontaneous symmetry breaking, we assign a random in-plane rotation to the initial $\boldsymbol{e}'_x$ ($\boldsymbol{e}'_y$). Furthermore, we introduce a constant angular velocity Ω_0, which is determined from the steady-state solution balancing the rotational drag torque and the electric torque (see Appendix D). The direction of $\boldsymbol{\Omega}_0$ ($\boldsymbol{e}'_x$) is restricted to lie in the plane by the torque $\boldsymbol{N}^\mathrm{C}$, computed from a harmonic potential U^C[30] (see Appendix B). The in-plane dipole axis $\boldsymbol{e}'_y$ is determined for all times as $\boldsymbol{e}'_y \equiv \boldsymbol{e}_z \times \boldsymbol{e}'_x$. For simplicity, instead of directly including the electric torque, we impose an additional constraint on the rotational degrees of freedom, see Equation (12). Specifically, we fix the rotational speed around $\boldsymbol{e}'_x$ to be Ω_0, while rotations around the other axes ($\boldsymbol{e}'_y$ and $\boldsymbol{e}'_z$) are unconstrained (see Appendix D).

The U_{ij}^S potential represents the excluded volume effect, and is described by a truncated $18-36$ Lennard–Jones potential, with a cut-off at $r_\mathrm{c} = 2^{1/18}\sigma$, with $\sigma = 2a$ the particle diameter. The potential U_{ij}^A is used to describe the electro-osmotic attraction, where the screening length is given by $\kappa = 1/(3\sigma)$.[16] This attractive force is caused by the electro-osmotic flow due to the Maxwell stress on the particle surface, where the Maxwell stress is induced by the applied DC electric field.[31] However, for simplicity, we ignore this flow and assume the attraction can be described with a simple isotropic potential, because the steady-state solution of the induced net dipole around the particle shows that the $P_\perp$ contribution is dominant compared to that of $P_\parallel$, see Appendices D and F. The strengths of the Lennard–Jones repulsion and electro-osmotic attraction are given by ϵ^LJ and ϵ^A, respectively. Finally, $\boldsymbol{F}^\mathrm{E}$ represents the (external) forces exerted by gravity and the wall, where the wall–particle interaction is again represented by a truncated Lennard–Jones potential, similar to the particle–particle steric interactions, that is chosen to be strong enough to exclude the particles from the wall.

We update the velocity field $\boldsymbol{u}$ and the particle motion $\boldsymbol{R}, \boldsymbol{V}, \boldsymbol{Q}$, and $\boldsymbol{\Omega}$ from Equations (7)–(12) (see Appendix C). We nondimensionalize all parameters, in particular, we define the nondimensionalized dipole components $\mu_\parallel \equiv P_\parallel/p_0$ and $\mu_\perp \equiv P_\perp/p_0$, respectively, where p_0 is the unit of the dipole strength, see Appendix E. In our simulations, taking advantage of our ability to fully resolve the flow field, we first focus on understanding the near-field effect of the HI. Therefore, we change $\mu_\parallel$ only, that is, Ω_0 and $\mu_\perp$ are fixed in the 2- and 3-body cases. On the other hand, in the simulations for many rollers, Ω_0 and $\boldsymbol{\mu}$ depend on the strength of the applied electric field E in accordance with the experimental system, see Appendix F.

3. Results

First, as an evaluation of the SP method, we confirm that the speed of the single roller is in good agreement with lubrication theory,[32,33] and that the flow field around the roller agrees with previous simulations that used a rotlet representation corrected by the Blake tensor[20,21,34,35] (see Appendix G). The self-propelling motion of a single roller is caused by the lubrication forces between rollers and the substrate, with the propulsion speed proportional to the angular velocity Ω_0 of the Quincke rotation. The advantage of the SP method is that it can accurately handle not only the lubrication force between a roller and the substrate but also HIs between rollers. We first focus on how the cluster states of two and three rollers are affected by these lubrication effects before later studying many-body systems.

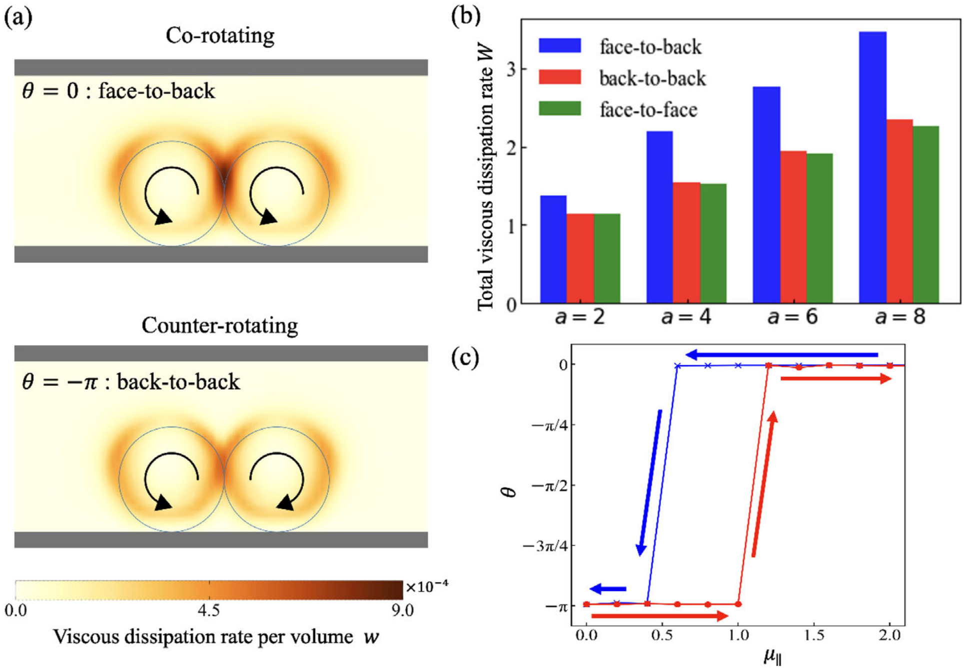

Figure 2. Behavior of a cluster consisting of two rollers. a) The viscous dissipation rate per volume, $w = [(\nabla \boldsymbol{u}) + (\nabla \boldsymbol{u})^{\mathrm{T}}]^2/2$, for the face-to-back ($\theta = 0$) and back-to-back ($\theta = -\pi$) states for radius $a = 8$ particles, where the blue circles represent the boundary line of each particle. The viscous dissipation in the space between the two rollers is higher than it is elsewhere, and the dissipation in the face-to-back state is larger than that in the back-to-back state. b) The counter-rotating (face-to-face or back-to-back) states dissipate less heat and might therefore be expected to be more stable than the co-rotating (face-to-back) state, based on the principle of minimum energy dissipation. Here, the face-to-face (back-to-back) state represents the case in which the two rollers are being propelled toward (away from) each other. Results shown for different roller sizes $a = 2$, 4, 6, and 8. c) Stable steady state for different dipole strengths draws a hysteresis curve, where $a = 2$. Arrows and colors in this curve indicate the direction of the loop. The HI stabilizes the back-to-back motion $\theta = -\pi$ at small $\mu_{\parallel}$, and the electrostatic interaction stabilizes the face-to-back motion $\theta = 0$ at large $\mu_{\parallel}$. Here, the strength of attraction sets $\epsilon = 10$, and all units are dimensionless, see Appendices E and F for more details.

3.1. 2-Body Case

The stable cluster states for 2-body systems can be classified into a co-rotating (face-to-back) state, in which the rollers are propelled in the same direction, $\theta = 0$, and a counter-rotating (face-to-face $\theta = \pi$ or back-to-back $\theta = -\pi$) state, in which they rotate in opposite directions, where θ is the relative angle between the axes of Quincke rotation of the rollers (see Movie S1 and Supporting Information and Supporting Information). In order to understand the stabilizing structure of clusters by HI, we consider the viscous dissipation of the system. The viscous dissipation of the fluid around the clusters in the co-rotating and counter-rotating states is shown in **Figure 2**a. The viscous dissipation rate is defined as $W = \int w(\boldsymbol{x})\mathrm{d}\boldsymbol{x}$ where the density $w(\boldsymbol{x}) = [(\nabla \boldsymbol{u}(\boldsymbol{x})) + (\nabla \boldsymbol{u}(\boldsymbol{x}))^T]^2/2$. According to the principle of minimum energy dissipation,[36–38] a nonequilibrium system prefers to be in a state with lower energy dissipation. In this system, the viscous dissipation in a counter-rotating state is lower than that in the co-rotating state, see Figure 2b. In addition, from the discussion regarding linear stability[39] and the forces acting between the rollers, we find that the back-to-back state is more stable than the face-to-back and face-to-face states due to the HI (see Supporting Information). On the other hand, the face-to-back state is stabilized by electrostatic interactions at the larger dipole strength. Surprisingly, this transition between face-to-back and back-to-back exhibits hysteresis-like behavior, see Figure 2c.

3.2. 3-Body Case

The behavior of the three-roller cluster can be explained by extending the analysis of the two-roller case. When the dipole interaction is weak, the HI stabilizes the immobile state, but when the dipole interaction is strong, the rotating cluster state is stabilized (see **Figure 3** and Movie S2, Supporting Information). This is a result of the dipole interaction stabilizing the rotation axis of each particle, either inward or outward relative to the geometric center of the cluster. To evaluate this quantitatively, we introduce a rotational order parameter for each cluster, $\Psi = \langle |\boldsymbol{n}_i \cdot \hat{\boldsymbol{r}'}_i| \rangle$, where $\langle \cdots \rangle$ denotes an average over the particles and time, the vector symbol $\hat{}$ represents a unit vector, the unit vector $\boldsymbol{n}_i$ refers to the axis of Quincke rotation for the i-th roller and $\boldsymbol{r}'_i = \boldsymbol{r}_i - \boldsymbol{r}_{\mathrm{G}}$, with $\boldsymbol{r}_{\mathrm{G}}$ being the center of mass of the cluster (see Supporting Information). A continuous transition is observed for the three-body cluster, between the immobile disordered clusters and the rotating clusters.

3.3. N-Body Case

In our simulations for a many-roller systems, we use steady-state solutions for the dipole and angular velocity, which depend on the electric field $E \equiv E_0/E_{\mathrm{Q}}$[9,40] (see Appendices D and F). The collective structures realized by the many-roller system can be

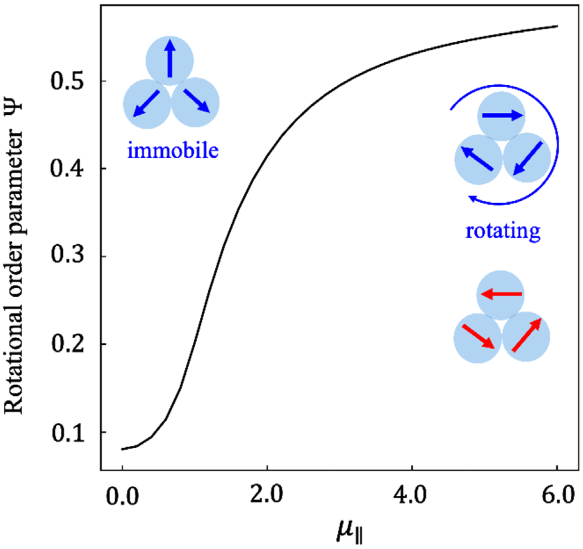

Figure 3. The rotational order parameter Ψ in a three-body system. When the dipole strength $\mu_{\|}$ is small, the HI propels the particles outward from each other, stabilizing the immobile state of the cluster. On the other hand, when $\mu_{\|}$ is large, the dipole interaction stabilizes the rotating cluster state.

classified by a set of order parameters[41] as follows (see Appendix H): polar liquid states (blue-outlined region), gas states (gray), vortex states (green), chain states (purple), rotating cluster states (orange), disordered cluster states (olive), and polar cluster states (azure) (see **Figure 4**, Movies S3 and S4, Supporting Information). When the applied electric field E is large enough, the rollers move away from each other, and as the area fraction increases, we can find two major order–disorder transitions: a transition from a disordered gas to an ordered polar liquid state and a transition from a polar liquid state to a disordered chain, gas or vortex state. On the other hand, when the electric field E_0 has an intermediate value, $E_0 \approx 2E_{\mathrm{Q}}$, a chain state is formed, and at increasing density ϕ_0, this chain state transitions to a vortex state. When the applied electric field E is small, each cluster is a rotating cluster state in the lower-density region, but as the density ϕ_0 increases, the clusters tend to become more anisotropic, colliding and coalescing repeatedly to form disordered clusters. At high enough density, all rollers form a single polar cluster.

4. Discussions

Our new 3D direct numerical simulation provides important insights into the relationship between particle interactions and collective dynamics. The major differences between our observed phase-diagram (see Figure 4) and previous simulation and experimental results[9,14,16] are the observation of the rotating cluster and chain states, as well as the vortex state at higher densities. Additionally, as one of the main features of the higher density region, the polar liquid state is transformed from an ordered phase into a disordered state, such as the gas and vortex states. This flocking transition can be considered to be influenced by the near-field HI we have discussed in 2- and 3-body cases.

We will now analyze the dominant physical mechanisms behind each of the transitions we have observed, for each of the main regions in the phase-diagram.

First, we discuss the transitions that occur upon increasing the applied electric field E_0, for example, $E_0 \approx 3E_{\mathrm{Q}}$ in Figure 4, where the repulsion due to $\mu_{\perp}$ eventually exceeds the attraction due to the electro-osmotic flow, causing the rollers to repel and move apart from each other. In this high electric field region, a disordered gas is observed in the dilute regions, that is, each roller propels independently, with no hydrodynamic or dipolar interaction induced cooperation, for $\phi_0 \leq 0.01$. As the area fraction ϕ_0 is increased, a transition from a disordered gas state to an ordered polar liquid state is observed, similar to the experimental results of Bricard et al.[9] Our flocking transition to a polar liquid state occurs near $\phi_0 \approx 0.01$, which is larger than $\phi_c \approx 3\times10^{-3}$ in the previous experiments by Bricard et al.[9] This difference may be due to the fact that in the experiment the rollers run on guide tracks, with left and right walls, which enhances rectification. Furthermore, the differences in the channel height H between our simulation $H/(2a) \approx 7$ and the experiment $H/(2a) \approx 50$ can lead to shifts in the critical densities ϕ_c at which these transitions occur. This is due to the fact that a change in the area fraction can be described by a corresponding change in the average interparticle distance $l \equiv a/\sqrt{\phi_0}$, see Supporting Information. As the area fraction ϕ_0 increases further, the distance l becomes smaller, and the transition from polar liquid states, which keep the balance between HIs and dipolar interactions, to the disordered gas, chain, and vortex states are observed in the denser regions $\phi_0 \geq 0.15$ ($l/a \leq 2.5$). This breaking of the polar liquid state is caused by an imbalance between the hydrodynamic and dipolar interactions, as the near-field HIs are more dominant than dipolar interactions in the dense regime, which is the case when $l/a \leq 2.5$ is close to the particle diameter scale. Our results suggest that the disordered dynamics of the active solid state observed by Geyer et al.[15] are caused by the polar liquid state disappearing at high density due to lubrication effects. However, unlike in the experiments, the solidification from polar liquid states has not been observed in our simulations.

Second, at $E_0 \approx 2.0E_{\mathrm{Q}}$ in Figure 4, our simulations show a chain state, for which we expect the electrostatic interactions to play an important role. There are three physical mechanisms behind this. First, the isotropic forces, which consist of the repulsive forces from the dipolar interaction $\mu_{\perp}$ and the attractive forces from the electro-osmotic flow, are balanced. Second, to avoid the interactions between chains, the average distance between particles $l/a \equiv 1/\sqrt{\phi_0}$ is less than the particle diameter, $l/a \leq 2.0$, that is, the density is smaller than 0.25. Finally, the dipolar interaction $\mu_{\|}$ dominates the HI, as discussed in the 2-body case (see the co-rotating case in Figure 2). By fulfilling these three conditions, the rollers can be attracted to each other to form a chain-like structure. Such a chain state has actually been observed in experiments,[42] though under different conditions to the preceding work.[9,16] More concretely, this experiment included a larger colloid size and different concentrations of conducting liquid, and in simulations, the chain state was observed for 2D active Brownian particles with dipole–dipole interactions (given by $\mu_{\|}$).[43]

Finally, our results provide new insights into the physical mechanisms responsible for various cluster motions observed

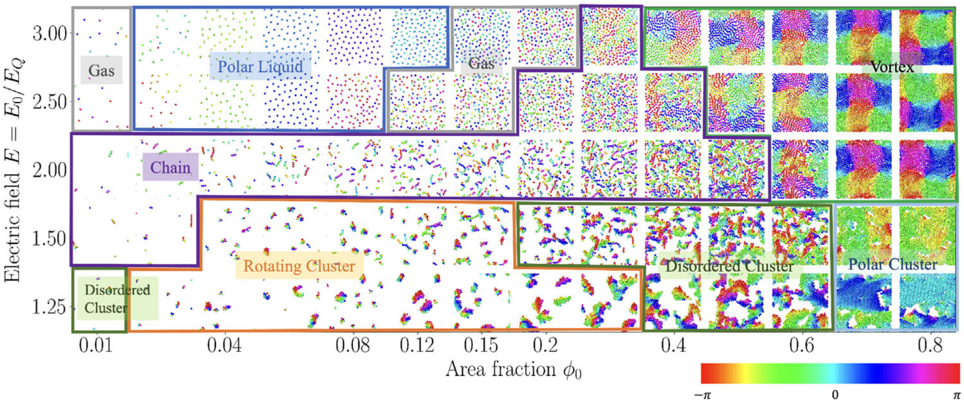

Figure 4. Phase diagram of a many-roller system (see Appendix H for the classifications of states by order parameters). The blue-outlined region represents polar liquid states, the gray-outlined region represents gas states, the green-outlined region represents vortex states, the purple-outlined region represents chain states, the orange-outlined region represents rotating cluster states, the olive-outlined region represents disordered cluster states, and the azure-outlined region represents polar cluster states. See Movies S3 and S4, Supporting Information, for representative examples of all of these phases.

in previous experiments.[14,16,18] In cluster motion, the attractive force due to the electro-osmotic flow plays an important role, where the direction of the force due to the flow is determined by the direction of the applied electric field.[31] That is, the flow creates an effective attractive interaction even if the systems do not strictly fulfill the criteria that the steady DC electric field $E_0 > E_{\mathrm{Q}}$, for example, under a periodic on–off field[14] or a subcritical DC field.[18] In our results, when the applied electric field E_0 is small, for example, $E_0 \approx 1.25E_{\mathrm{Q}}$ in Figure 4, the attraction due to the electro-osmotic flow is dominant and the cluster motion is reproduced. From the fact we can observe a rotating cluster, as discussed for the 3-body case in Figure 3, we can infer that the dipolar interactions are dominant compared the near-field HIs over the whole density region, that is, the cluster is stabilized by the dipolar interactions over the viscous dissipation effect of the near-field HIs. In the transition from the rotating cluster to the disordered and polar clusters at high density, the relative strength of each interaction hardly changes, because the relative distances between particles show no significant change. Therefore, the differences in the shape of the cluster are important when classifying the type of motion. A cluster with an isotropic shape tends to be a rotating cluster, with the rotating motion created by stabilization through $\mu_{\parallel}$, see Figure 3. A disordered cluster has an anisotropic shape (e.g., elliptical), which tends to form at denser regions, because these isotropic shaped clusters are broken by frequently collapsing with each other, and a polar cluster state consists of a single system-spanning cluster, which eventually results in a global translational motion. Such collisions and mergers between clusters happen approximately at a density $\phi_0 \geq 0.25$, where the average distance between particles $l/a \equiv 1/\sqrt{\phi_0}$ is larger than or equal to the particle diameter, similar to the chain state.

5. Conclusion

In conclusion, we take advantage of DNS to investigate the flocking transition mechanism of Quincke rollers and their dynamics in the high-density regime. The DNS of the fluid flow is performed using the SP method, a simulation method that can resolve the many-body HIs of dense dispersions and the explicit flow field. Our DNS findings for 2- and 3-body systems reveal that the near-field HIs change the directions of the rotational axis into disordering states. Specifically, the counter-rotating state is stabilized in the 2-body case, and the immobile cluster is formed in the 3-body case. The hydrodynamic effect is dominant when the interparticle distance is on the diameter scale, and can be quantitatively evaluated by the viscous dissipation. For the collective dynamics, we observe new collective behavior that has not been seen in previous simulations: a chain, rotating cluster, and vortex states. Our DNS show that the near-field HIs play a crucial role to disrupt the alignments of the roller rotations for the polar liquid state in the high density regime under high electric fields, giving rise to disordered collective behavior such as gas and vortex states. As already known, the balance between hydrodynamic and electrostatic coupling is important as a physical mechanism for such collective behavior, however, our DNS clarifies the relationship between the balance of these couplings and the collective behaviors, that is, we reveal which coupling is dominant for each of the observed collective modes in the phase diagram. Concretely, the near-field HIs are more dominant than dipolar interactions in the transition from polar liquid to disordered states at high electric field and high densities. On the other hand, at low electric field strengths the dipolar interactions given by the induced dipole moments $\mu_{\parallel}$ on the flat wall are dominant, compared to the near-field HIs, producing the chain and the rotating cluster states. The electrostatic couplings are dominant over all density regions at low electric field strength, because the near-field HIs are smaller due to the the slower Quincke rotation. Therefore, the cluster states, which are formed by the attractive force due to the electro-osmotic flow around each roller, exhibit a transition upon increasing the area fraction. This transition is caused by the deformation of the cluster shape, from isotropic to anisotropic, due to the frequent collision and merger of clusters in the dense region. Our proposed DNS method can be easily extended to the collective dynamics of microrollers in magnetic fields.[21,44] Our findings show that the HIs differ between the near and far fields, which indicates the possibility of new improvements in particle-based models.

Appendix A: Derivation of Forces and Torques from the Potential

The potential U depends not only on the relative position of the particles $\boldsymbol{r}$ but also on their relative orientations in space, as given by the rotation axis for Quincke rotation and the dipole moments of the particles. The interparticle forces and torques can be obtained from the potential as follows[26]

$$F^{\mathrm{P}} = -\frac{\partial U}{\partial \boldsymbol{r}} \tag{A1}$$

$$N^{\mathrm{P}} = -\sum_m \hat{a}_m \times \frac{\partial U}{\partial \hat{a}_m} \tag{A2}$$

where the $\hat{a}_i$ are the (body-fixed) orthonormal principal axis vectors ($m = x', y', z'$).

Appendix B: A Torque to Constrain the Quincke Rotation

We introduce an external torque inspired by a Quincke roller. It has been analytically proven that the angular velocity vector generated by Quincke rotation is perpendicular to the external electric field $\boldsymbol{E}_0$.[11] In our model, to simplify the treatment, we impose a constant angular velocity vector $\boldsymbol{\Omega}_0$ on a rigid sphere and a constraint torque $\boldsymbol{N}^{\mathrm{C}}$ defined by a harmonic potential U^{C} is introduced to maintain the rotation axis in the plane, see **Figure B1**. Specifically, the constraint potential U^{C} and torque $\boldsymbol{N}^{\mathrm{C}}$ are defined from the directions of $\boldsymbol{E}_0$ and $\boldsymbol{\Omega}_0$ as follows:

$$U^{\mathrm{C}} = \frac{K}{2}\left(\hat{\boldsymbol{E}}_0 \cdot \hat{\boldsymbol{\Omega}}_0\right)^2 = \frac{K}{2}\left(\boldsymbol{e}_z \cdot \boldsymbol{e}'_x\right)^2 \tag{B1}$$

$$\boldsymbol{N}^{\mathrm{C}} = K\left(\hat{\boldsymbol{E}}_0 \cdot \hat{\boldsymbol{\Omega}}_0\right)\left(\hat{\boldsymbol{E}}_0 \times \hat{\boldsymbol{\Omega}}_0\right) = K\left(\boldsymbol{e}_z \cdot \boldsymbol{e}'_x\right)\left(\boldsymbol{e}_z \times \boldsymbol{e}'_x\right) \tag{B2}$$

where the vector symbol $\hat{}$ denotes a unit vector, $\boldsymbol{e}_z \equiv \hat{\boldsymbol{E}}_0$, and $\{\boldsymbol{e}'_x, \boldsymbol{e}'_y, \boldsymbol{e}'_z = \boldsymbol{e}_z\}$ define a time-dependent orthonormal basis (the Quincke-frame). The initial $\boldsymbol{e}'_x$ is set to be randomly oriented in the plane parallel to the electrode (perpendicular to $\boldsymbol{e}_z$), where we define $\boldsymbol{e}'_y \equiv \boldsymbol{e}_z \times \boldsymbol{e}'_x$ and $\boldsymbol{\Omega}_0 = \Omega_0 \boldsymbol{e}'_x$. Physically, the direction of the dipole is determined from a small perturbation due to the spontaneous symmetry breaking of the surface charge distribution, see main text. $K > 0$ is the amplitude of the constraint torque, whose value must be sufficiently larger than the sum total of the remaining torques, that is, the hydrodynamic $\boldsymbol{N}^{\mathrm{H}}$ and others $\boldsymbol{N}^{\mathrm{P}}$, because the axis of rotation should be fixed. The constraint torque $\boldsymbol{N}^{\mathrm{C}}$ is obtained from the potential as $\hat{\boldsymbol{\psi}} \cdot \boldsymbol{N}^{\mathrm{C}} = -\frac{\partial U^{\mathrm{C}}}{\partial \psi} = -\frac{\partial U^{\mathrm{C}}}{\partial \hat{\boldsymbol{\Omega}}_{\mathrm{c}}} \cdot \frac{\partial \hat{\boldsymbol{\Omega}}_0}{\partial \psi}$, where ψ is the angle around the unit axis vector $\hat{\boldsymbol{\psi}}$, where we use the rotation formula $\frac{\partial \hat{\boldsymbol{\Omega}}_0}{\partial \psi} = \hat{\boldsymbol{\Omega}}_0 \times \hat{\boldsymbol{\psi}}$.[30]

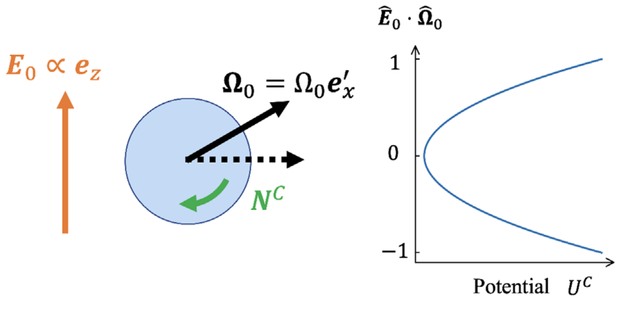

Figure B1. A schematic diagram of the torque is used to constrain the axis of rotation. The angle between the applied electric field $\boldsymbol{E}_0$ and the angular velocity by the Quincke rotation $\boldsymbol{\Omega}_0$ is constrained to be perpendicular by a harmonic potential U^{C}. Here, the $\{\boldsymbol{e}'_x, \boldsymbol{e}'_y, \boldsymbol{e}'_z = \boldsymbol{e}_z\}$ define a time-dependent orthonormal basis (the Quincke-frame). The initial $\boldsymbol{e}'_x$ is set to be randomly oriented in the plane parallel to the electrode (perpendicular to $\boldsymbol{e}_z$), where we define $\boldsymbol{e}'_y \equiv \boldsymbol{e}_z \times \boldsymbol{e}'_x$ and $\boldsymbol{\Omega}_0 = \Omega_0 \boldsymbol{e}'_x$. The black solid arrows give the orientation an $\boldsymbol{\Omega}_0$ perturbed by extra torques due to interparticle interactions, that is, $\boldsymbol{N}^{\mathrm{H}}$ and $\boldsymbol{N}^{\mathrm{P}}$, and the dotted arrows show the preferred orientation due to the constraint $\boldsymbol{N}^{\mathrm{C}}$.

Appendix C: Simulation Procedure

First of all, to obtain the time evolution of the total velocity $\boldsymbol{u}$, we employ a fractional-step approach, effectively dividing Equation (7) in two[24]

$$(\partial_t + \boldsymbol{u} \cdot \nabla)\boldsymbol{u} = \rho_{\mathrm{f}}^{-1} \nabla \cdot \boldsymbol{\sigma} \tag{C1}$$

$$\partial_t \boldsymbol{u} = \phi \boldsymbol{f}_{\mathrm{p}} \tag{C2}$$

where the first equation accounts for the advection and viscous stresses, while the second gives the constraint required to maintain the rigidity of the particles, with both updates satisfying the divergence-free condition. We use the following computational algorithm to solve this time evolution.

The numerical solution of our method uses a fractional-step approach, and the simulation procedure at the n-th time step $t_n = n\Delta t$ is as follows:[23,24]

1) We obtain ϕ^n and $\boldsymbol{u}^n$ from the configuration $\{\boldsymbol{R}_i^n\}$ and the velocities $\{\boldsymbol{V}_i^n\}$ and $\{\boldsymbol{\Omega}_i^n\}$, where the superscript n denotes the time step, and then we calculate $\boldsymbol{u}^\star$ using $\boldsymbol{u}^n$ as,

$$\boldsymbol{u}^\star = \boldsymbol{u}^n + \int_{t_n}^{t_n+\Delta t} \nabla \cdot \left[\rho_{\mathrm{f}}^{-1}\boldsymbol{\sigma} - \boldsymbol{u}\boldsymbol{u}\right] \mathrm{d}t' \tag{C3}$$

where $\boldsymbol{\sigma} = -\nabla p^\star + \eta_{\mathrm{f}}[\nabla \boldsymbol{u} + (\nabla \boldsymbol{u})^{\mathrm{T}}]$ is the stress; $(\cdots)^{\mathrm{T}}$ indicates a transpose and the pressure $p^\star$ is determined to fulfill the incompressibility condition $\nabla \cdot \boldsymbol{u}^\star = 0$.

2) We update the configuration $\{\boldsymbol{R}_i^n, \boldsymbol{Q}_i^n\}$ to $\{\boldsymbol{R}_i^{n+1}, \boldsymbol{Q}_i^{n+1}\}$ using the velocities $\{\boldsymbol{V}_i^n, \boldsymbol{\Omega}_i^n\}$ and obtain the updated ϕ^{n+1}.
3) We calculate the hydrodynamic force $\boldsymbol{F}_i^{\mathrm{H}}$ and torque $\boldsymbol{N}_i^{\mathrm{H}}$ from the updated profile function ϕ^{n+1} and then further calculate the forces $\boldsymbol{F}_i^{\mathrm{P}}$, $\boldsymbol{F}_i^{\mathrm{E}}$ and torques $\boldsymbol{N}_i^{\mathrm{P}}$, $\boldsymbol{N}_i^{\mathrm{C}}$ due to the interparticle interactions and external field.
4) From the forces and torques, we obtain the updated velocities $\{\boldsymbol{V}_i^{n+1}\}$ and $\{\boldsymbol{\Omega}_i^{n+1}\}$.
5) The particle velocity field $\boldsymbol{u}_{\mathrm{p}}^{n+1}$ is updated and then the velocity field $\boldsymbol{u}$ is determined from the momentum impulse by imposing the rigid-body constraint on the particle velocity field,

$$\boldsymbol{u}^{n+1} = \boldsymbol{u}^\star + \int_{t_n}^{t_n+\Delta t} \phi \boldsymbol{f}_{\mathrm{p}} \mathrm{d}t' \tag{C4}$$

$$\int_{t_n}^{t_n+\Delta t} \phi \boldsymbol{f}_{\mathrm{p}} \mathrm{d}t' = \phi^{n+1}\left(\boldsymbol{u}_{\mathrm{p}}^{n+1} - \boldsymbol{u}^\star\right) - \frac{\Delta t}{\rho_{\mathrm{f}}} \nabla p_{\mathrm{p}} \tag{C5}$$

where the impulse by $\phi \boldsymbol{f}_{\mathrm{p}}$ in Equation (C5) is balanced by the momentum change due to particle motion, and p_{p} is the pressure, which acts as a Lagrange multiplier to fulfill the incompressibility condition $\nabla \cdot \boldsymbol{u}^{n+1} = 0$, that is, the pressure obeys the Poisson equation, $\nabla^2 p_{\mathrm{p}} = \rho_{\mathrm{f}} \nabla \cdot \{\phi(\boldsymbol{u}_{\mathrm{p}}^{n+1} - \boldsymbol{u}^\star)\}/\Delta t$. The total pressure p^{n+1} can be obtained as $p^{n+1} = p^\star + p_{\mathrm{p}}$.

6) We return to step 1.

The equations of motion are solved using the second-order Adams–Bashforth method. The time step is taken to be $\Delta t = \rho_{\mathrm{f}}/(\eta_{\mathrm{f}} k_{\mathrm{max}}^2)$, where $k_{\mathrm{max}} = 2\pi/\Delta$ is the maximum wavenumber.

Appendix D: The Induced Electric Dipole Moments and Rotation Speed for the Steady-State Quincke Rotation

Let us consider the correspondence between the theoretical and simulation parameters. In Quincke rotation, the equations of rotational motion for the single particle and the time evolution of an electric dipole, under an applied DC electric field, are written as follows:[9,11,40]

$$\boldsymbol{I} \cdot \frac{\mathrm{d}\boldsymbol{\Omega}}{\mathrm{d}t} = \boldsymbol{P} \times \boldsymbol{E}_0 - (\mu_\mathrm{r})^{-1}\boldsymbol{\Omega} \tag{D1}$$

$$\frac{\mathrm{d}\boldsymbol{P}}{\mathrm{d}t} + \frac{1}{\tau}\boldsymbol{P} = -\frac{1}{\tau}2\pi\epsilon_0 a^3 \boldsymbol{E}_0 + \boldsymbol{\Omega} \times \left(\boldsymbol{P} - 4\pi\epsilon_0 a^3 \chi^\infty \boldsymbol{E}_0\right) \tag{D2}$$

where $\mu_\mathrm{r} = (8\pi\eta_\mathrm{f}a^3)^{-1}$ is the rotational mobility of a spherical particle, $\tau \equiv \frac{\epsilon_\mathrm{p}+2\epsilon_\mathrm{l}}{2\sigma_\mathrm{l}}$ is the Maxwell–Wagner time, and $\chi^\infty \equiv \frac{\epsilon_\mathrm{p}-\epsilon_\mathrm{l}}{\epsilon_\mathrm{p}+2\epsilon_\mathrm{l}}$, with ϵ_p and ϵ_l the dielectric permittivities of the sphere and the liquid medium, respectively, σ_l is the conductivity of the liquid medium and ϵ_0 is the dielectric permittivity of vacuum.

The steady-state solution for the dipole moment induced in a dielectric sphere can be expressed as follows:

$$P_\perp = P_\perp^\epsilon E - \frac{P_\perp^\sigma}{E},\ P_\parallel = P_\perp^\sigma\sqrt{1 - \frac{1}{E^2}} \tag{D3}$$

where $E \equiv E_0/E_\mathrm{Q}$, $P_\perp^\epsilon \equiv 4\pi\epsilon_0 a^3 \chi^\infty E_\mathrm{Q}$ is the static contribution from the dielectric polarization, and the z-component $P_\perp^\sigma \equiv \epsilon_0/(\tau\epsilon_\mathrm{l}\mu_\mathrm{r}E_\mathrm{Q})$ and the xy-component $P_\parallel$ are the dynamic contributions from the Quincke rotation for $E > 1$, where E_Q the threshold value for Quincke rotation. Additionally, the angular velocity of a roller in the steady state is described as

$$\Omega_0 = \frac{1}{\tau}\sqrt{E^2 - 1} \tag{D4}$$

Note that the accuracy of this approximation, obtained from the steady-state solutions, is guaranteed when the unit of time t_0 is sufficiently longer than the Maxwell–Wagner time τ, for example, $t_0 \gg \tau$ (see the paragraph on units for a definition of the unit t_0). As a result of this solution, we can implement the Quincke rotation effect simply by introducing an angular velocity $\boldsymbol{\Omega}_0$, with constant magnitude, which is the steady-state solution and depends on the strength of the applied electric field. More explicitly, instead of directly including $\boldsymbol{N}^\mathrm{Q}$, we fix the rotation around the x'–axis to be Ω_0, whereas rotations around the y'- and z'-axes are free, and computed to satisfy the torque-free conditions. The Quincke-coordinates $(\boldsymbol{e}_x', \boldsymbol{e}_y', \boldsymbol{e}_z')$ have been introduced in Appendix B. Thus, we constrain the rotational motion for our Quincke rollers to be of the form $(\boldsymbol{\Omega}_0, \boldsymbol{\Omega}_{y'}, \boldsymbol{\Omega}_{z'})$, in the coordinate system (x', y', z').

Appendix E: Units

Within the SP method, the system is discretized on a rectangular grid with spacing Δ, under periodic boundary conditions in all directions. This allows us to employ a pseudo-spectral method, and significantly reduce the computational cost. The units of all variables are based on the fundamental simulation parameters Δ, η_f and ρ_f, the grid spacing, fluid viscosity, and fluid density, respectively. The unit of length is $l_0 = \Delta$, time $t_0 = \rho_\mathrm{f}\Delta^2/\eta_\mathrm{f}$, and that of energy is $e_0 = \eta_\mathrm{f}^2\Delta/\rho_\mathrm{f}$. The electric dipole is measured in units of $p_0 = \sqrt{4\pi\epsilon_0 e_0 l_0^3}$. Here, the viscosity of the liquid is $\eta_\mathrm{f} \approx 4.3 \times 10^{-3}$ Pa·s, the density ratio between the colloids and the liquid is $\rho_\mathrm{p}/\rho_\mathrm{f} = 1.19/0.77 \approx 1.5$,[12] the dielectric permittivities $\epsilon_\mathrm{p} \approx 2.6\epsilon_0$,[11] $\epsilon_\mathrm{l} \approx 2.0\epsilon_0$,[45] and the ratio $\chi^\infty \approx 0.08$.[9] Based on these physical quantities, we can estimate the parameter units to be $l_0 = \Delta = 1\,\mu\mathrm{m}$, $t_0 = \frac{\rho_\mathrm{f}\Delta^2}{\eta_\mathrm{f}} \approx 0.1\,\mu\mathrm{s}$, $e_0 = \frac{\eta_\mathrm{f}^2\Delta}{\rho_\mathrm{f}} \approx 10^{-14}$ J, and $p_0 = \sqrt{4\pi\epsilon_0 e_0 l_0^3} \approx 10^{-21}$ C·m. Because the Maxwell–Wagner time $\tau \approx 1$ ms,[9] the accuracy of the steady-state solutions Equations (D3) and (D4) is not sufficiently guaranteed in this unit t_0. However, to simplify the problem and to build our fundamental understanding in the collective system, we proceed with the simulation under the assumption that the contribution from the steady-state is dominant.

Appendix F: Simulation Parameters

We set the simulation parameters from these theoretical values, and we define $\mu_\parallel$ and $\mu_\perp$ as the dimensionless dipole components corresponding to $P_\parallel$ and $P_\perp$, respectively, where in what follows all units are dimensionless. The system size is $(L_x, L_y, L_z) = (128, 128, 32)$. We introduce a flat wall parallel to the xy plane at $z = 0$, with a total depth of $d = 5$, that is, the distance H between the top/bottom surfaces is constant for all simulations. We set the height H to fulfill $H/\pi \geq 2a$ for $a = 2$, and use $H = 27$ for all simulations. This characteristic distance H/π plays an important role in determining the HIs between rollers, because the HI switches, at the interparticle distance s, between the near-field ($s < H/\pi$, the boundary effect of the top wall is negligible) and the far-field ($s \geq H/\pi$, the boundary effect of the top wall should be considered).[9] That is, for our system $(H/\pi)/(2a) \approx 2$, the near-field HI is dominant when the particle are separated by distances on the order of their diameters, and the far-field HI is valid when the particles are sufficiently far apart, that is, on distances larger than at least twice their diameters. The condition $H/\pi \geq 2a$ guarantees that our simulations can consider both near- and far-field HIs, additionally, in practice, a smaller H will also reduce the computational cost. The particle Reynolds number is defined as $Re \equiv \rho_\mathrm{f}\sigma^2\Omega_0/\eta_\mathrm{f}$, and $Re \approx 10^{-5}$ in experiments,[9,12] where we assume that $Re \approx 1$ to reduce the computational cost. Because the excluded volume effect is sufficiently larger than the electro-osmotic attraction, we set $\epsilon \equiv \epsilon^\mathrm{LJ} = \epsilon^\mathrm{A}$ for simplicity, and we take the interfacial width of the particle domain to be $\xi = 2$ for optimal accuracy.[24] In order to focus on the roller motion on the substrate, we keep the distance between rollers and substrate constant during the simulation. For this, we have set the gravity acting on the rollers to be $g = 1$, substantially larger than the value of 10^{-7} suggested by the analysis of simulation units. For one, two, and three roller simulation, we set $Re = 1$. To investigate the stable structures of cluster states in the simulation for two and three rollers, we assume that the strength of the repulsive force $\mu_\perp = 0$, and that of the attractive force $\varepsilon = 10.0(30.0)$ for two (three) rollers, in order to stabilize the cluster motion. We choose as radius $a = 2, 4, 6,$ and 8 for the two roller systems and $a = 2$ for the three roller ones. Additionally, for many-rollers simulations, we set $a = 2$, the strength of the attractive force $\epsilon = 10.0$, and the area fraction is varied in the range $\phi_0 = 0.01 - 0.8$, based on the steady-state solution of Equations (D3) and (D4). Each input parameter is determined from the electric field E as follows: the angular velocity is $\Omega_0 \approx 0.025 \times \sqrt{E^2 - 1}$, the dipole moment is $\mu_\parallel \approx 2.6 \times \sqrt{1 - \frac{1}{E^2}}$, and the ratio between the dipole components is $|\mu_\perp|/|\mu_\parallel| \approx E$.

Appendix G: Numerical Validations

We present a numerical validation for the propulsion of a microroller. The propulsion speed $v_0/(\Omega_0 a)$ as a function of the distance between the surface of the particle and the wall is derived from lubrication theory[32,33] as follows:

$$f^\mathrm{tr} = \begin{cases} \frac{1}{8}\left(\frac{a}{h}\right)^4\left(1 - \frac{3}{8}\frac{a}{h}\right) & \left(\frac{a}{h} \ll 1\right) \\ \frac{2}{15}\ln\left(\frac{\delta}{h}\right) + 0.25726 + \frac{86}{375}\left(\frac{\delta}{a}\right)\ln\left(\frac{\delta}{h}\right) & \left(\frac{\delta}{a} \ll 1\right) \end{cases} \tag{G1}$$

$$f^\mathrm{tt} = \begin{cases} -\left[1 - \frac{9}{16}\left(\frac{a}{h}\right) + \frac{1}{8}\left(\frac{a}{h}\right)^3 - \frac{45}{256}\left(\frac{a}{h}\right)^4 - \frac{1}{16}\left(\frac{a}{h}\right)^5\right]^{-1} & \left(\frac{a}{h} \ll 1\right) \\ -\frac{8}{15}\ln\left(\frac{\delta}{h}\right) + 0.95429 - \frac{64}{375}\left(\frac{\delta}{a}\right)\ln\left(\frac{\delta}{h}\right) & \left(\frac{\delta}{a} \ll 1\right) \end{cases} \tag{G2}$$

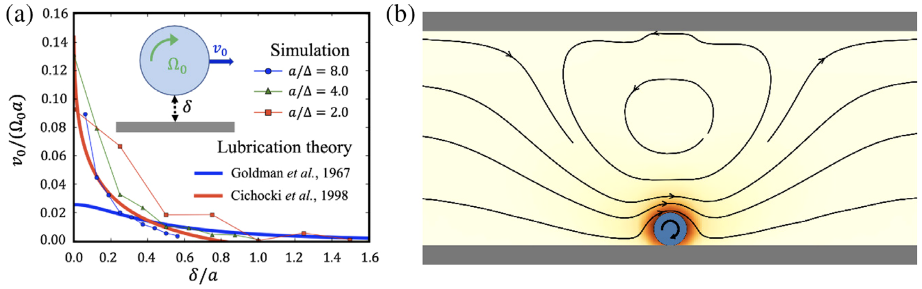

Figure G1. a) Normalized roller velocity $v_0/(a\Omega_0)$ as a function of the distance between the surface of the particle and the wall, δ, for comparison with lubrication theory (far field: Goldman et al., 1967; near field: Cichocki et al., 1998). b) Flow field around a single roller.

where $h = a + \delta$. We define F^{t} as the drag force acting on the particle for translational motion and F^{r} as the translational hydrodynamic force for a rotating particle; these forces are defined as $F^{\mathrm{tt}} = 6\pi\mu a f^{\mathrm{tt}}(\delta) v_0$ and $F^{\mathrm{tr}} = 6\pi\mu a^2 f^{\mathrm{tr}}(\delta)\Omega_0$. Since the forces acting on the particle satisfy the force-free condition, $F^{\mathrm{tt}} + F^{\mathrm{tr}} = 0$, we obtain the relation $v_0(\delta)/(\Omega_0 a) = -f^{\mathrm{tr}}(\delta)/f^{\mathrm{tt}}(\delta)$. Our simulations using the SP method can reproduce the results of lubrication theory, and the accuracy increases as the particle radius increases; see **Figure G1**a. This relation has been confirmed in experiments on Quincke rollers by Pradillo et al.[12] and is a sufficiently reliable result. Note that the propulsion speed v_0 and lubrication forces F^{tr}, F^{tt} are proportional to the angular velocity Ω_0 because the distance δ is constant, thanks to the large value of gravity, as detailed in Appendix F.

The flow field around a single roller appears as shown in Figure G1b. This flow field reproduces the results of the multiblob method with a rotlet corrected by the Blake tensor.[21,34,35] Here, we perform computations for a system that accounts for the effects between the upper and lower wall surfaces, which is slightly different from the system treated in the multiblob method. In the multiblob method, the mobility matrix is computed via the superposition of two-body interactions based on the Stokesian dynamics method,[20] whereas in our SP method, the hydrodynamic equations are treated precisely by direct numerical calculation.

Appendix H: Classification of Collective Behavior by Order Parameters

To characterize each state, we define a polar order parameter (POP), a bond-orientational order parameter (BOP), a rotational order parameter (ROP), and a chain order parameter (COP),[41] and we show the corresponding fingerprints of each state (see **Figure H1**). Note that the POP is defined as the average of the propulsion directions of all particles, $|\langle \boldsymbol{n}_i \rangle|$, where $\boldsymbol{n}_i$ is the unit vector of Quincke rotation axis of the i-th roller and $\langle\cdots\rangle$ denotes an average over the particles and time, while the BOP and COP reflect whether the particles are arranged in a hexagonal configuration or a straight line. The BOP is defined as $\langle|\psi_i|\rangle$,

$$\psi_i = \sum_{j=1}^{Z_i} \exp(i6\theta_{ij})/Z_i \tag{H1}$$

where Z_i is the coordination number of the i-th particle obtained from a Voronoi construction for the particle configuration and θ_{ij} is the angle between a reference axis and the bond between the i-th particle and its j-th neighbor. A value $\psi = 1$ indicates perfect hexagonal ordering, whereas a completely disordered structure corresponds to $\psi = 0$. The ROP is defined as $\langle|\langle \hat{\boldsymbol{\Omega}}_{0,i} \cdot \hat{\boldsymbol{r}'}_i \rangle_{\mathrm{c}}|\rangle$, where $\langle\cdots\rangle_{\mathrm{c}}$ denotes taking the average for the particles that make up each cluster in each snapshot, and the operation $\langle\cdots\rangle$ denotes taking the average over the values for each cluster. Here, we use the relative position vector $\boldsymbol{r}'_i = \boldsymbol{r}_i - \boldsymbol{r}_{\mathrm{G}}$, with $\boldsymbol{r}_{\mathrm{G}}$ being the center of gravity for each cluster, where a cluster is defined as a set of rollers that are in contact with each other. The COP is defined as $\langle c_i \rangle_{\mathcal{M}} \equiv \sum_{i=1}^{\mathcal{M}} c_i/\mathcal{M}$,

$$c_i = \frac{1}{{}_{\mathcal{N}_i}C_2} \sum_{(j,k)\in S_i, j\neq k} \left[\frac{2}{3}\left(\frac{1}{2} - \frac{\boldsymbol{r}_{ij}\cdot\boldsymbol{r}_{ik}}{r_{ij}r_{ik}}\right)\right] \tag{H2}$$

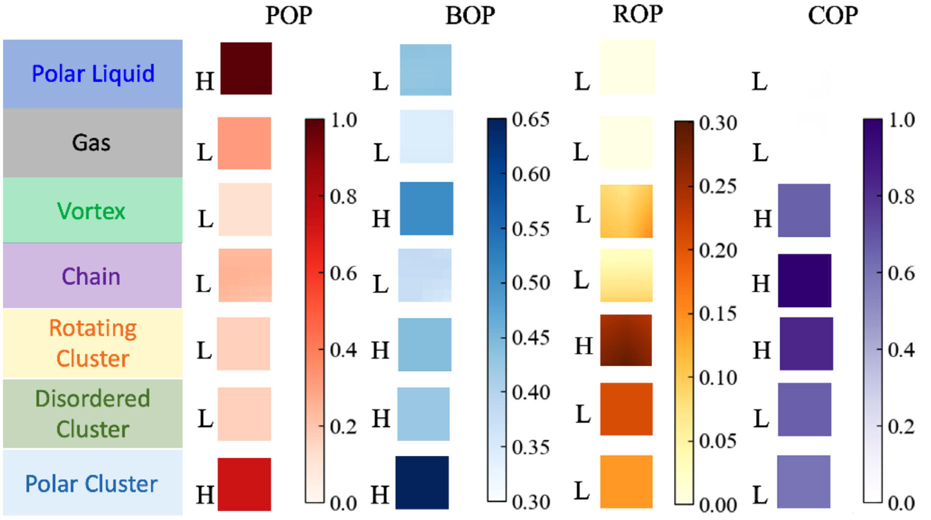

Figure H1. Fingerprints of each state are created by the order parameters. The polar order parameter (POP), the bond-orientational order parameter (BOP), the rotational order parameter (ROP), and the chain order parameter (COP) are used to classify the states. The letters "H" and "L" denote high and low values of the order parameters, respectively, and the threshold values are defined as 0.6 (POP), 0.40 (BOP), 0.25 (ROP), and 0.6 (COP).

where $\mathcal{M}$ represents the number of particles that are in contact with two or more other particles, $\mathcal{N}_i$ is the number of particles in contact with the i-th particle, and $\mathcal{S}_i$ denotes the region where other particles are in contact with the i-th particle, that is, a circle with a radius on the order of the particle diameter centered on the i-th particle.[41]

Supporting Information

Supporting Information is available from the Wiley Online Library or from the author.

Acknowledgements

This work was supported by Grants-in-Aid for Scientific Research (JSPS KAKENHI) under grant nos. JP 20H00129, 20H05619, and 20K03786. It was also supported by Professional development Consortium for Computational Materials Scientists (PCoMS). R.Y. acknowledges helpful discussions with Profs. Hajime Tanaka and Akira Furukawa.

Conflict of Interest

The authors declare no conflict of interest.

Author Contributions

All authors designed the research and wrote the paper. S.I., K.S., and R.Y. performed the simulations and analyzed the data. J.J.M. assisted with numerical methods.

Data Availability Statement

The data that support the findings of this study are available from the corresponding author upon reasonable request.

Keywords

active matter, collective motion, hydrodynamic effect, Quincke roller, smoothed profile method

Received: September 20, 2022
Revised: January 13, 2023
Published online: February 3, 2023

---

[1] T. Vicsek, A. Zafeiris, *Phys. Rep.* **2012**, *517*, 71.
[2] M. C. Marchetti, J.-F. Joanny, S. Ramaswamy, T. B. Liverpool, J. Prost, M. Rao, R. A. Simha, *Rev. Mod. Phys.* **2013**, *85*, 1143.
[3] J. Elgeti, R. G. Winkler, G. Gompper, *Rep. Prog. Phys.* **2015**, *78*, 056601.
[4] A. Zöttl, H. Stark, *J. Phys.: Condens. Matter* **2016**, *28*, 253001.
[5] G. Gompper, R. G. Winkler, T. Speck, A. Solon, C. Nardini, F. Peruani, H. Löwen, R. Golestanian, U. B. Kaupp, L. Alvarez, T. Kiørboe, E. Lauga, W. C. K. Poon, A. DeSimone, S. Muiños-Landin, A. Fischer, N. A Söker, F. Cichos, R. Kapral, P. Gaspard, M. Ripoll, F. Sagues, A. Doostmohammadi, J. M. Yeomans, I. S. Aranson, C. Bechinger, H. Stark, C. K. Hemelrijk, F. J. Nedelec, T. Sarkar, *J. Phys.: Condens. Matter* **2020**, *32*, 193001.
[6] A. Snezhko, *Curr. Opin. Colloid Interface Sci.* **2016**, *21*, 65.
[7] M. Driscoll, B. Delmotte, *Curr. Opin. Colloid Interface Sci.* **2019**, *40*, 42.
[8] H. Xie, M. Sun, X. Fan, Z. Lin, W. Chen, L. Wang, L. Dong, Q. He, *Sci. Rob.* **2019**, *4*, 28.
[9] A. Bricard, J.-B. Caussin, N. Desreumaux, O. Dauchot, D. Bartolo, *Nature* **2013**, *503*, 95.
[10] G. Quincke, *Ann. Phys.* **1896**, *295*, 417.
[11] N. Pannacci, L. Lobry, E. Lemaire, *Phys. Rev. Lett.* **2007**, *99*, 094503.
[12] G. E. Pradillo, H. Karani, P. M. Vlahovska, *Soft Matter* **2019**, *15*, 6564.
[13] S. Q. Lu, B. Y. Zhang, Z. C. Zhang, Y. Shi, T. H. Zhang, *Soft Matter* **2018**, *14*, 5092.
[14] H. Karani, G. E. Pradillo, P. M. Vlahovska, *Phys. Rev. Lett.* **2019**, *123*, 208002.
[15] D. Geyer, D. Martin, J. Tailleur, D. Bartolo, *Phys. Rev. X* **2019**, *9*, 031043.
[16] A. Mauleon-Amieva, M. Mosayebi, J. E. Hallett, F. Turci, T. B. Liverpool, J. S. van Duijneveldt, C. P. Royall, *Phys. Rev. E* **2020**, *102*, 032609.
[17] B. Zhang, H. Karani, P. M. Vlahovska, A. Snezhko, *Soft Matter* **2021**, *17*, 4818.
[18] Z. T. Liu, Y. Shi, Y. Zhao, H. Chaté, X.-q. Shi, T. H. Zhang, *Proc. Natl. Acad. Sci. U. S. A.* **2021**, *118*, 40.
[19] J. W. Swan, J. F. Brady, *Phys. Fluids* **2007**, *19*, 113306.
[20] F. Balboa Usabiaga, B. Kallemov, B. Delmotte, A. Bhalla, B. Griffith, A. Donev, *Commun. Appl. Math. Comput. Sci.* **2017**, *11*, 217.
[21] M. Driscoll, B. Delmotte, M. Youssef, S. Sacanna, A. Donev, P. Chaikin, *Nat. Phys.* **2017**, *13*, 375.
[22] M. R. Shaebani, A. Wysocki, R. G. Winkler, G. Gompper, H. Rieger, *Nat. Rev. Phys.* **2020**, *2*, 181.
[23] R. Yamamoto, J. J. Molina, Y. Nakayama, *Soft Matter* **2021**, *17*, 4226.
[24] Y. Nakayama, R. Yamamoto, *Phys. Rev. E* **2005**, *71*, 036707.
[25] Y. Nakayama, K. Kim, R. Yamamoto, *Eur. Phys. J. E: Soft Matter Biol. Phys.* **2008**, *26*, 361.
[26] M. P. Allen, G. Germano, *Mol. Phys.* **2006**, *104*, 3225.
[27] A. Aguado, P. A. Madden, *J. Chem. Phys.* **2003**, *119*, 7471.
[28] M. P. Allen, D. J. Tildesley, *Computer Simulation of Liquids*, Oxford University Press, Oxford **2017**.
[29] K. A. Dwelle, A. P. Willard, *J. Phys. Chem. C* **2019**, *123*, 24095.
[30] H. Goldstein, C. Poole, J. Safko, *Classical Mechanics*, American Association of Physics Teachers, Maryland **2002**.
[31] Y. Solomentsev, M. Böhmer, J. L. Anderson, *Langmuir* **1997**, *13*, 6058.
[32] A. J. Goldman, R. G. Cox, H. Brenner, *Chem. Eng. Sci.* **1967**, *22*, 637.
[33] B. Cichocki, R. Jones, *Phys. A* **1998**, *258*, 273.
[34] J. Blake, A. Chwang, *J. Eng. Math.* **1974**, *8*, 23.
[35] B. Delmotte, *Phys. Rev. Fluids* **2019**, *4*, 044302.
[36] J. W. Strutt, *Proc. London Math. Soc.* **1871**, *1*, 357.
[37] L. Onsager, *Phys. Rev.* **1931**, *37*, 405.
[38] L. Onsager, *Phys. Rev.* **1931**, *38*, 2265.
[39] E. Lauga, *The Fluid Dynamics of Cell Motility*, Vol. *62*, Cambridge University Press, Cambridge **2020**.
[40] D. Das, D. Saintillan, *Phys. Rev. E* **2013**, *87*, 043014.
[41] S. Imamura, T. Kawakatsu, *Eur. Phys. J. E: Soft Matter Biol. Phys.* **2021**, *44*, 1.
[42] L. López Llobet, A. Fernández-Nieves, *Bachelor Theses*, Universitat de Barcelona **2020**.
[43] G.-J. Liao, C. K. Hall, S. H. Klapp, *Soft Matter* **2020**, *16*, 2208.
[44] A. Kaiser, A. Snezhko, I. S. Aranson, *Sci. Adv.* **2017**, *3*, e1601469.
[45] J. Schmidt, R. Prignitz, D. Peschka, A. Münch, B. Wagner, E. Bänsch, W. Peukert, *J. Colloid Interface Sci.* **2012**, *386*, 240.